A Mechanical Model of Early Somite Segmentation

Priyom Adhyapok[1], Agnieszka M Piatkowska[2], Michael J Norman[3],

Sherry G Clendenon[1], Claudio D Stern[2], James A Glazier[1], Julio M Belmonte[3*]

[1]*Indiana University Bloomington, USA;* [2]*UCL, United Kingdom;* [3]*NC State University, USA*

corresponding author: jbelmon2 @ncsu.edu

Abstract:

The clock-and-wavefront model (CW) hypothesizes that the formation of somites in vertebrate embryos results from the interplay of molecular oscillations with a wave traveling along the body axis. This model however does not explain how molecular information is interpreted by cells to modulate their rearrangement into somites. Here we performed Scanning Electron Microscopy (SEM) on the pre-somitic mesoderm (PSM) of chicken embryos at stages 11-12 to describe in detail the cell shape changes occurring along the axis of the PSM. This reveals a wave of epithelialization of the dorsal PSM that precedes somite segmentation. Signs of spatially periodic apical constriction appear in this layer starting at least 3-4 somite lengths caudal to the most recently formed somite. The sizes of these clusters correspond to the typical diameter of chicken somites. We propose that a mechanical instability process leads to the separation of cells into these structures and positions the future inter-somite boundaries. We present a model in which a wave of apical constriction leads to increasing tension and periodic failure of adhesion junctions within the dorsal epithelial layer of the PSM, thus positioning somite boundaries.

25 *This model can produce spatially periodic segments whose size depends on the speed*

26 *of the contraction wave (W) and the rate of increase of apical contractility (Λ). The Λ/W*

27 *ratio determines whether this mechanism produces spatially and temporally regular or*

28 *irregular segments, and whether segment sizes increase with the wave speed (scaling)*

29 *as in the CW model. We discuss the limitations of a purely mechanical model of somite*

30 *segmentation and the role of biomechanics along with CW during somitogenesis.*

31

32 **Keywords:** Somitogenesis, biomechanics, mesenchymal-epithelial transition,

33 mechanical instability, segmentation

34

35

INTRODUCTION

37

38 Somitogenesis in vertebrate development sequentially and periodically creates

39 metameric epithelial balls (somites) along the elongating embryo body from bilateral

40 rods of loosely connected mesenchymal cells called pre-somitic mesoderm (PSM). As

41 cells leave the rostral/anterior (head) end of the PSM to form each somite, new cells

42 continuously move from the tail bud to join the PSM at the caudal/posterior (tail) end of

43 the embryo [1]. At any given rostral-caudal position, a pair of nearly equal-sized somites

44 form simultaneously on both sides of the neural tube, between the ectoderm and the

45 endoderm. These transient structures are the precursors of vertebrae, ribs and many

46   skeletal muscles; many birth defects are associated with a failure in one or more steps

47   in this long developmental process [2].

48

49   Somitogenesis is strikingly robust to perturbations (both spatial and temporal). Changes

50   in the total number of embryonic cells or in the rate of new cell addition at the caudal

51   end lead to compensating changes in the size and timing of somite formation so that the

52   embryo eventually produces the same final number of somites as in normal

53   development [3-4]. One way to achieve this conservation of final somite number is for

54   the size of the somites to increase linearly (*scale*) with the speed of the caudal-moving

55   position of the determination front or with the rate at which cells join the caudal end of

56   the PSM.

57

58   Models seeking to explain somite formation include the 'cell cycle model', which couples

59   the timing of segmentation to the progression of cells through the cell-cycle and a cell-

60   intrinsic gating mechanism [5-7] and reaction-diffusion models [8-9]. Currently, the most

61   widely accepted family of models employ a 'clock and wavefront' (CW) mechanism

62   which combines caudally progressing waves of determination and differentiation with an

63   intracellular oscillator which determines cell fate based on its phase at the moment of

64   determination [10]. Following the identification of the first oscillating transcripts (*hairy1*

65   and *hairy2*) in the PSM [11], many computer simulations of varying complexity have

66   implemented different CW models. Most CW models reproduce the experimentally

67   observed scaling of somite size with clock period, wavefront speed and rate of

68   elongation of the PSM [12-14].

69

70 Recent experiments have shown that somite-like structures can form without either a

71 clock or a wavefront [9,15]. The ability of somites to form without either a clock or a

72 wavefront suggests that we should consider other mechanisms that could lead to

73 spatially and temporally periodic sequential division of the PSM into regular segments.

74 Moreover, recent experiments by Nelemans and colleagues showed that applied

75 tension along the rostral-caudal axis can induce the formation of intersomitic boundaries

76 in locations not specified by CW signaling [16], suggesting that mechanical mechanisms

77 may be important in generating intersomitic boundaries.

78

79 In 2009, Martins and colleagues imaged the morphology of cells during chicken

80 somitogenesis *in vivo*, showing that cells elongate, crawl and align with each other as

81 they form a somite [17]. Importantly, their observations show that cells epithelialize

82 gradually during somite formation, with epithelialization beginning before segments

83 separate from each other. This finding is consistent with other reports showing that PSM

84 cells gradually increase the density of cell-cell adhesion molecules [18] and decrease

85 their motility [19-20] as they approach the time of the physical reorganization associated

86 with somite formation. Moreover, several decades ago, scanning electron microscopy

87 (SEM) observations of the PSM in a variety of species led to the suggestion that "pre-

88 somite" like structures, named "somitomeres", precede the condensation of cells into

89 somites by at least 2-3 somite lengths [21-22]. However, these observations were made

90 mostly in randomly fractured embryos along various planes and it is difficult to

91 determine the progression of somitogenesis from them.

92

93   Here we took a new look at the PSM cells to investigate this early organization in more

94   detail. Consistent with previous work, our observations show that dorsal PSM cells

95   undergo an early maturation process, forming an epithelial monolayer along the

96   ectoderm boundary, beginning long before somite formation. This pre-somitic epithelium

97   also shows signs of a pre-segmentation process, with cohorts of cells forming arched

98   tissue segments of roughly the length of a somite diameter.

99

100   These observations suggest that periodic tissue segmentation and somite boundary

101   positioning could result from a mechanical instability mechanism, similar to what is seen

102   in periodic cracking of materials subjected to stress. We developed a model of the

103   dorsal epithelial monolayer where the observed boundaries between dorsal segments

104   arise from the break of contact between neighboring cells due to increased apical

105   tension between cells. We simulated this scenario with a 2D computational model of a

106   cross-section of the epithelial monolayer and showed that spatial periodicity in segment

107   sizes can be explained by a simple mechanical model without a clock. We also showed

108   that this model can produce either constant-size segments or segments whose size

109   increases (*scales*) with wave speed and inverse rate of increase of apical contractility. A

110   roughly constant ratio of the wave speed to apical contractility build-up rate defines the

111   boundary between these two domains. A second ratio also predicts when this

112   mechanism produces spatially and temporally regular segments from irregular

113   segments.

114

115

116   **RESULTS**

117

118   ***Early signs of boundary specification***

119

120   To investigate the beginning of epithelialization, we performed 3D Scanning Electron

121   Microscopy (SEM) of chick embryos fixed at various stages of somitogenesis, fractured

122   as precisely as possible along parasagittal or transverse planes [27]. We then manually

123   defined the contour of each individual PSM cell and calculated their aspect ratios

124   (Figure 1A,B).

125

126   Our observations show that a dorsal layer of PSM cells begins to epithelialize at least as

127   early as 4-5 somite-lengths caudal to the most recently formed somite (S1).

128   Furthermore, cells within this dorsal epithelium form a series of cohorts at least 3-4

129   somite lengths caudal to the forming somite (Figure 1A). Cells near the dorsal surface

130   within these cohorts are usually wedged shaped, with their apical (ventral facing) sides

131   more constricted than their basal (dorsal facing) sides. The sizes of these cohorts are

132   regular and roughly correspond to the rostral-caudal length of the future somites.

133
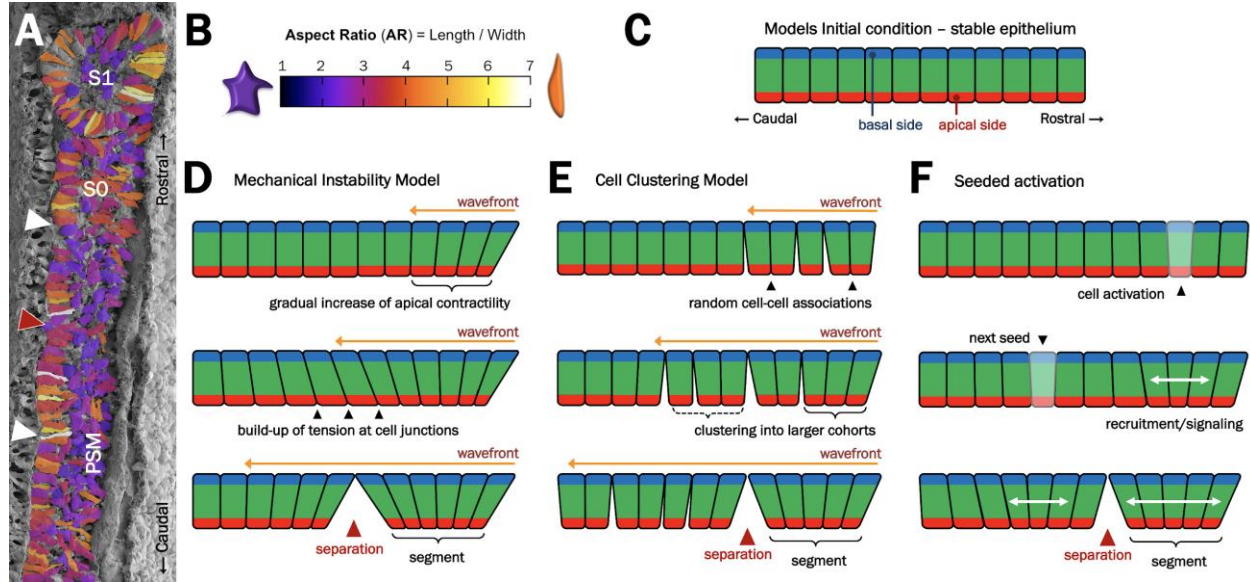
Figure 1 – Early signs of pre-somitic epithelium segmentation and proposed models of segment formation

(**A**) SEM images of para-sagittally sectioned chicken embryos shows the epithelialization of dorsal PSM cells at least 5 somite-lengths caudal (left) to the S1 somite. Cells are colored according to their aspect ratio, as shown in (**B**). White arrowheads show the positions of segment boundaries. (**C**-**F**) Models of mechanical-instability mechanism of tissue segmentation. (**C**) Epithelialized cells, with defined apical (red) and basal (blue) sides form a rostral (right)-caudal (left) monolayer along the dorsal side of the PSM. (**D**) Mechanical instability model: a caudal-moving wavefront of myosin activation (orange arrows) initiates apical constriction of the cells in the monolayer eventually leading to the periodic segmentation of the tissue. (**E**) Cell condensation model: a caudal-moving wavefront of maturation (orange arrows) initiates random cell-cell groupings that eventually organizes the tissue into regularly sized cohorts. (**F**) Seeded activation mechanism: instead of a continuous wave, small groups of cells are activated and rearrange neighboring cells into a segment.

A mechanical model of dorsal PSM pre-patterning for segmentation

151

152 The correlation between cohort size with somite rostral-caudal length and tear

153 positioning with projected somite boundaries suggest that these structures are

154 precursors of the future inter-somite boundary. But how do they arise? Figure 1D-F

155 illustrates some possible mechanistic models, including a cell clustering model with a

156 continuous wavefront (Fig. 1E) and other variations where changes in cell behaviors do

157 not progress continuously from caudal to rostral (Fig. 1F).

158

159 Here, we take the convergence of the cells' apical sides within the cohort as an

160 indication that cells are undergoing apical constriction as the PSM matures. Apical

161 constriction is the result of contractile forces generated by myosin activity at the cells'

162 apical side, which often bring neighboring cells together and give them a wedge shape

163 [28-32]. It is known that when apical contractile forces exert too much load on junctional

164 adhesion sites, tissue tears appear, as observed in *Drosophila* embryos [33-34]. We

165 postulate that this mechanism - a mechanical instability model - may be behind the pre-

166 segmentation pattern we observe: a caudally travelling activation wave induces apical

167 constriction along the maturing PSM cells (Figure 1D), leading to a buildup of cell-cell

168 apical tension (Figure 1E) that eventually subdivides the monolayer into regularly sized

169 segments (Figure 1F). This is the model we explore in this paper.

170

171 The model has three main variables: the speed at which this caudally-travelling wave

172 passes through the tissue (W), the rate at which each pair of activated cells increases

173 its apical contractility (Λ), and the maximum tension a cell pair can sustain before the

174   cells break their connection to each other (T_{break}). For any given value of T_{break}, we

175   expect average segment sizes to increase proportionally with W and inversely with Λ. In

176   the following subsections we implement two different versions of this model to explore

177   whether and under which conditions this process can produce spatially and temporally

178   regular segments.

179

180   ***Linear elastic model of tissue segmentation***

181

182   We first implemented the mechanical model of the interaction between adjacent cells in

183   the dorsal monolayer as a series of springs connecting a chain of point objects. The

184   model creates motion by linearly increasing the spring constant over time at rate Λ, with

185   a delay between spring activation based on how far along the chain the spring is (W). At

186   each time step, the acceleration due to spring forces is calculated and used to set up a

187   system of $2N$ first order ordinary differential equations (ODEs) with time dependent

188   coefficients, where N is the number of cells (points) in the system. If at any given time

189   step the tension of a spring exceeds T_{break}, the spring constant is set to zero for the

190   remainder of the simulation, effectively breaking the spring. The time and location of

191   each break is recorded. For more details on the model implementation, see

192   *Computational Models*.

193

194   For short times, each cell pair tension evolves with the same patterns, first increasing

195   roughly linearly over time after activation, until eventually turning over, decreasing for a

196   short time and increasing again at a slower rate (Supplemental Figure 1A). During this

197   process, the subsequent cell pair tensions follow a similar pattern, but time-delayed and

198   reaching higher tensions before turning over. Eventually one spring reaches the

199   threshold tension, setting the first break. We found the size (or position) of the first

200   break, which we call the segment size (S), to be proportional to W and inversely

201   proportional to Λ, as expected (Supplemental Figure 1B).

202

203   However, after the first break happens and tension is lost on one side of the monolayer,

204   the cell centers (the point objects) begin to collapse quickly and the cell positions start

205   to overlap (Supplemental Figure 1C). From there onwards the physical requirement that

206   the order of the cells must be preserved is no longer guaranteed and the subsequent

207   breaking points lose their biological meaning. Addition of spring resting lengths and

208   ceilings on the maximum spring constant did not improve the oscillatory behavior and

209   cell position overlaps after the first break.

210

211   ***A Cellular Potts implementation of the mechanical instability model***

212

213   The above results suggest that a more realistic representation of the dorsal cells that

214   takes into account cell shapes, viscosity and thermal fluctuations, is needed for the

215   implementation of a mechanical instability model of tissue segmentation. In the

216   subsections that follow we implemented a stochastic Cellular Potts Model

217   (CPM)/Glazier-Graner-Hogeweg (GGH) model version of the dorsal tissue

218   segmentation process. (For more details see *Computational Models*) In this model, the

219   cells are not points, but spatially extended objects similar to the schematic cells in

220   Figure 1C-F with a width and height; apical, basal and core domains; and elastic

221   connections between neighboring apical domains that follows the same rules as in the

222   purely elastic model. We first characterize the model behavior with different values of a

223   fixed spring constant (λ_A) and simultaneous rate of increase of apical contractility on all

224   cells (Λ) before exploring the gradual, caudally-moving wavefront of apical constriction

225   activation.

226

227   ***Tension profiles as a function of number of cells and constriction strength***

228

229   We first test our model by creating small epithelial monolayers composed of 4 to 16

230   cells of fixed aspect ratio $AR = 2$ (Figure 2A). The strength of apical contractility of all

231   cell pairs was increased simultaneously at a fixed build up rate of $\Lambda = 0.05$, from $\lambda_A = 0$

232   up to a maximum value of $\lambda_A = 600$, without allowing apical links to break. We then

233   observe the shape of the tissue and the average cell pair tension (Eq. 6) over 20,000

234   simulation time units (defined in terms of Monte Carlo Steps (MCS)), after λ_A has

235   reached its maximum value. As the number of cells in the monolayer increases, cell

236   pairs in the middle of the segment are under higher tension compared to cell pairs near

237   the periphery (Figure 2B,C). This forms the premise of our model - as the tissue

238   becomes larger, more tension is accumulated between cell pairs, thus predisposing the

239   tissue to break into smaller segments when a breaking tension threshold is present.

240
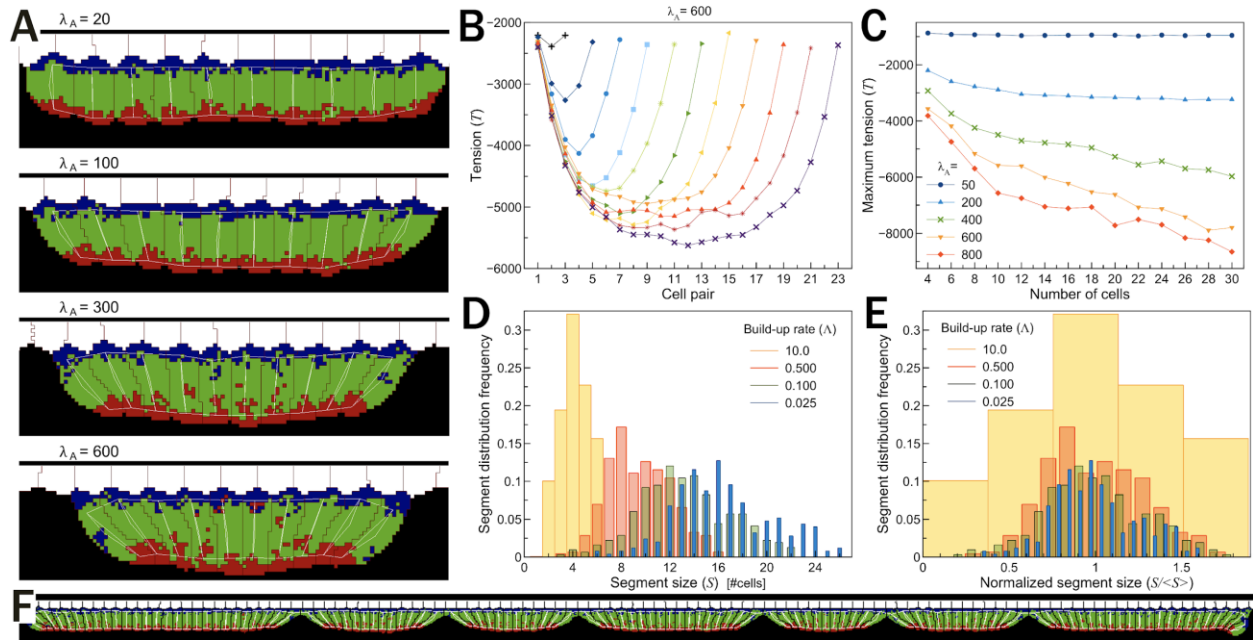
Figure 2 - Tension and segment size distributions for fixed tissue sizes and simultaneous increase in contractility

(**A**) Snapshots of 4 simulations of 10 cells with different levels of maximal apical contractility strength. The tissue becomes more constricted with larger values of λ_A. (White - ectodermal tissue; black - non-modeled PSM; cells domain colors as in Figure 1C-F; vertical white lines - internal distance constraints between cell domains (Eq. 3); horizontal white lines - distant constraints between domains of neighboring cells (Eq. 5)). (**B**) Plot of average apical tension (Eq. 6) between cell pairs at the end of multiple simulations with different numbers of cells (from 4 to 24). In all these simulations λ_A is set to 600. (**C**) Plot of maximum cell pair tension versus the number of cells in the tissue for different maximal values of λ_A. (**D-E**) Histogram of distribution of segment sizes (**D**) and normalized segment sizes (**E**) for different build-up rates of apical contractility. (**F**) Snapshot of a simulation with $\Lambda = 0.05$ showing a wide distribution of segment sizes.

Simultaneous activation of apical contractility leads to irregularly sized segments

258   Next, we combine the simultaneous activation with the breaking of the apical links by

259   imposing a tension threshold $T_{break} = -7500$ after which the link between the apical

260   domains of neighboring cells is broken. As in the previous section, in these simulations

261   the strength of apical contractility is increased linearly from $\lambda_A = 20$ up to a maximum

262   value of $\lambda_A = 600$ at different rates of apical contractility build-up ($\Lambda = d\lambda/dt$). Since now

263   any cell contact is initially equally susceptible to break, we obtain a broad distribution of

264   segment sizes (Figure 2D-F), with the average segment size increasing as the build-up

265   rate decreases (Figure 2D). The shape of the distribution, however, remains the same

266   for all values of Λ (Figure 2E), except when the rates are bigger than 10, where we

267   found that most cell pairs break. The data in Figure 2D-F are from simulations with

268   periodic boundary conditions, but the results are qualitatively the same for simulations

269   with a large number of cells ($N > 400$) and fixed boundaries (Supplemental Figure 2).

270   We conclude that a simultaneous activation of constriction activity is insufficient to

271   produce a regular pattern of pre-segments similar to those seen in our SEM

272   observations of embryos (Figure 1A).

273

274   ***Gradual and sequential activation of apical contractility leads to tissue***
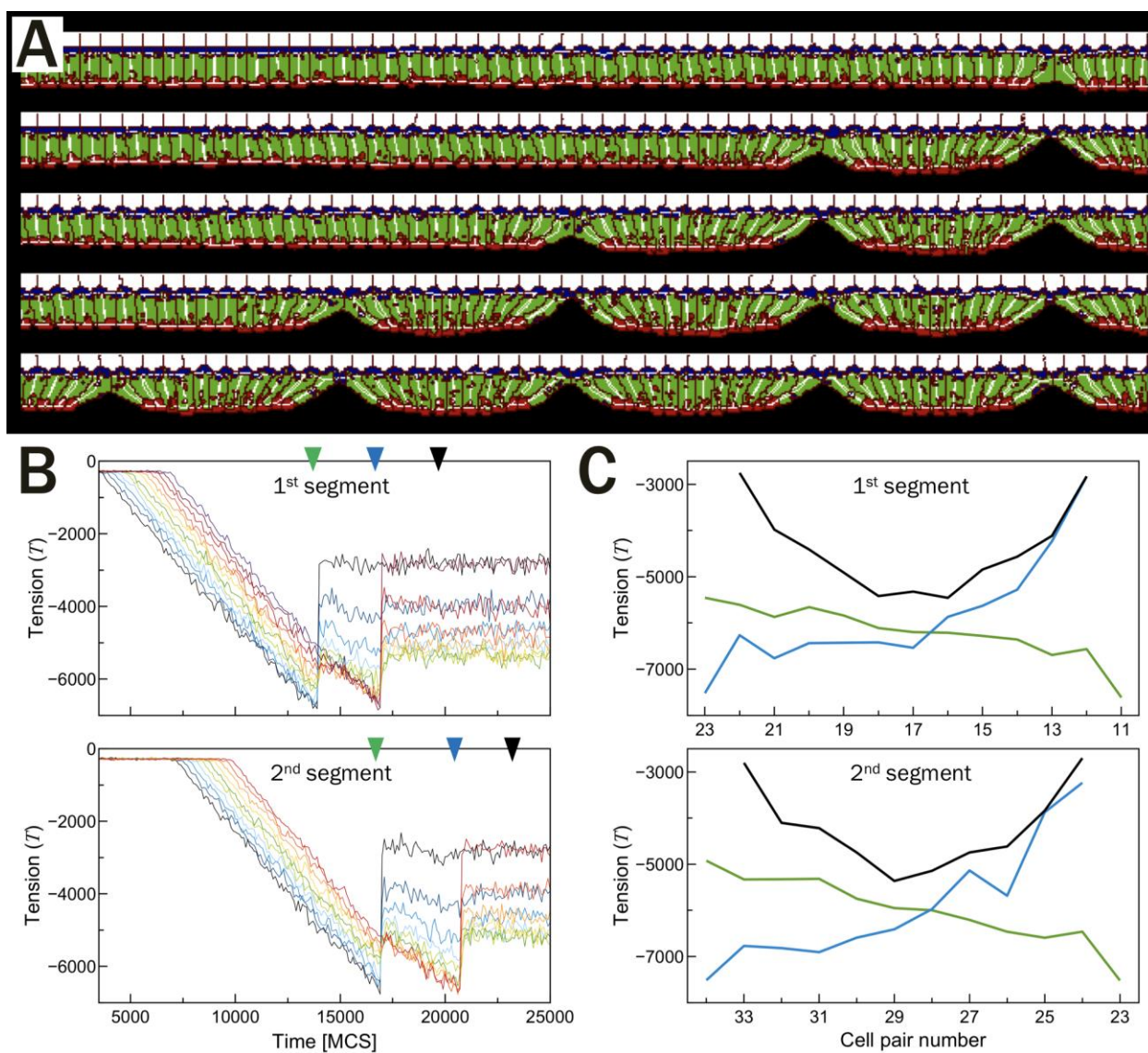
275   ***segmentation***

276

277   Next, we investigated whether sequential activation of apical constriction can slice a

278   tissue to generate regularly sized segments. From now on, all simulations have a large

279   number of cells and a caudally moving front of activation that sequentially initiates a

280   gradual and linear increase of the strength of apical contractility of cell pairs. The wave

281   speed W and build-up rate of apical contractility Λ will be varied systematically around

282   their base values (see Table1). In addition, apical cell pairs will have a maximum

283   tension load T_{break}, after which their links break and a tear may appear between the

284   apical region of those cells.

285

286   Figure 3A shows a time series of a zoomed-in section of a simulation with 115 cells

287   where 4 tissue segments form. With the exception of the first and last two segments

288   (due to boundary conditions), all segments are of similar size ($<S>= 11.36 +/- 1.45$)

289   and segmentation occurs at similar time intervals ($<\tau>= 3442.37 +/- 587.87$) for our

290   standard set of parameter values (see Table1). We also looked at the evolution of the

291   tension profile for 2 sequential segments. As the wavefront of activation passes, the

292   tension between cell pairs gradually increases, with the rostral-most pair with the higher

293   tension (Figure 3B and green lines in Figure 3C). After the formation of the rostral-most

294   boundary/tear the pattern inverts, with the rostral-most cell pairs now more relaxed and

295   the caudal-most pairs now under higher tension (compare green and blue lines in

296   Figure 3C). Formation of the caudal-most boundary relaxes the tension of these pairs

297   and the segment tension profile has now a symmetrically convex shape with an average

298   lower tension compared with the intermediate steps (black lines in Figure 3C). The

299   same process repeats itself in the formation of the subsequent segments.

300

Figure 3 - Tissue segmentation from a caudally propagating wave initiating apical constriction

(**A**) Time-series of a simulation showing the sequential segmentation of a tissue due to a linear increase of apical cytoskeletal activity as cells are progressively activated from rostral (right) to caudal (left). Colors as in Figure 3A and parameters are from Table 1. Snapshots taken at the approximate moment the separation occurs (17000, 21000, 24000, 28000 and 31000 MCS). (**B**) Time evolution of cell pair tensions in the regions of 2 consecutive segments. Lines are plotted beginning with the rostral-most pair of cells for each segment. (**C**) Tension profiles for the 2 tissue segments shown in (**B**). Each line corresponds to the same-color arrowheads in (**B**) and indicate three different events - formation of the rostral segment

310   boundary (green), formation of caudal segment boundary (blue), and some time after the caudal event

311   occurs (black).

312

313

314   ***Segment size scaling with wave speed and rate of apical constriction***

315

316   The clock and wavefront model was proposed to explain how somite size can adjust to

317   variations of embryo size [10]: all else being equal, a faster clock produces smaller

318   somites, while a faster wavefront generates larger somites. We now investigate if our

319   mechanical model of segmentation has the same scaling features: does a faster wave

320   of activation (W) lead to larger segments? How does average segment size change with

321   different build-up rates of apical contractility (Λ)? In the results that follow we

322   systematically varied both parameters and all data points were averaged over 5

323   simulation replicas.

324

325   We first fixed the build-up rate of apical contractility Λ and varied the wave speed W. We

326   observe two regimes of the average segment size $< S >$ with respect to the wave

327   speed. For wave speeds below a critical value ($< W^*$) average segment size $< S^* >$

328   was constant, but increased as a power law with exponents close to ¼ for faster wave

329   speeds ($> W^*$) (Figure 4A). The critical values of the wave speed W^* and average

330   segment size $< S^* >$ for the change from constant segment size to the scaling regime

331   depends on the value of the build-up rate Λ (Figure 4B). These results suggest that the

332   discrete spatial compartmentalization of the tissue in cell units poses a lower limit on

333   segment size as a function of Λ (Figure 4B). In fact, our simulations in absence of a

334   wave already indicate that the maximum tension a cell pair can reach depends on the

335   number of cells within a forming segment (Figure 2B), so for slow waves we expect the

336   tears to always occur at regular size intervals.

337

338   The average distance between apical constriction activation and boundary formation $<$

339    $D >$ showed a less surprising behavior with an approximate linear scaling with wave

340   speed (Figure 4C): the faster the wave, the larger the distance between the wavefront

341   and the boundaries. Changes in the base value of Λ only shifted the curves, with lower

342   build-up rates increasing the distance between activation and boundary formation. The

343   average time interval between the formation of successive boundaries $< \tau >$ depends

344   only on W, and not on Λ, with faster wave speeds decreasing the segmentation time as

345   a power law with exponent -0.80 ± 0.008 (Figure 4D).

346

347   Next we fixed the wave speed W and varied the build-up rate of apical contractility Λ.

348   Average segment sizes $< S >$ decrease logarithmically with higher build-up rates, but

349   became constant after a critical value of Λ^* (Supplemental Figure 3A,B). As before,

350   segment sizes outside the scaling regime ($< S^* >$) depends on the value of the wave

351   speed W used in the simulations (Supplemental Figure 3B). Again, these results can be

352   understood in light of the way cell pair tension increases with segment size (Figure 2B).

353   For slow build-up rates ($< \Lambda^*$), the sole factor determining segment size is the wave

354   speed, with faster waves adding more cells to the forming segment before the boundary

355   formation (Figure 4A). For higher build-up rates ($> \Lambda^*$), however, the rate of cell addition

356   is not fast enough to overcome the increase in tension profile, which itself is a function

357   of tissue size (Figure 2B).

358
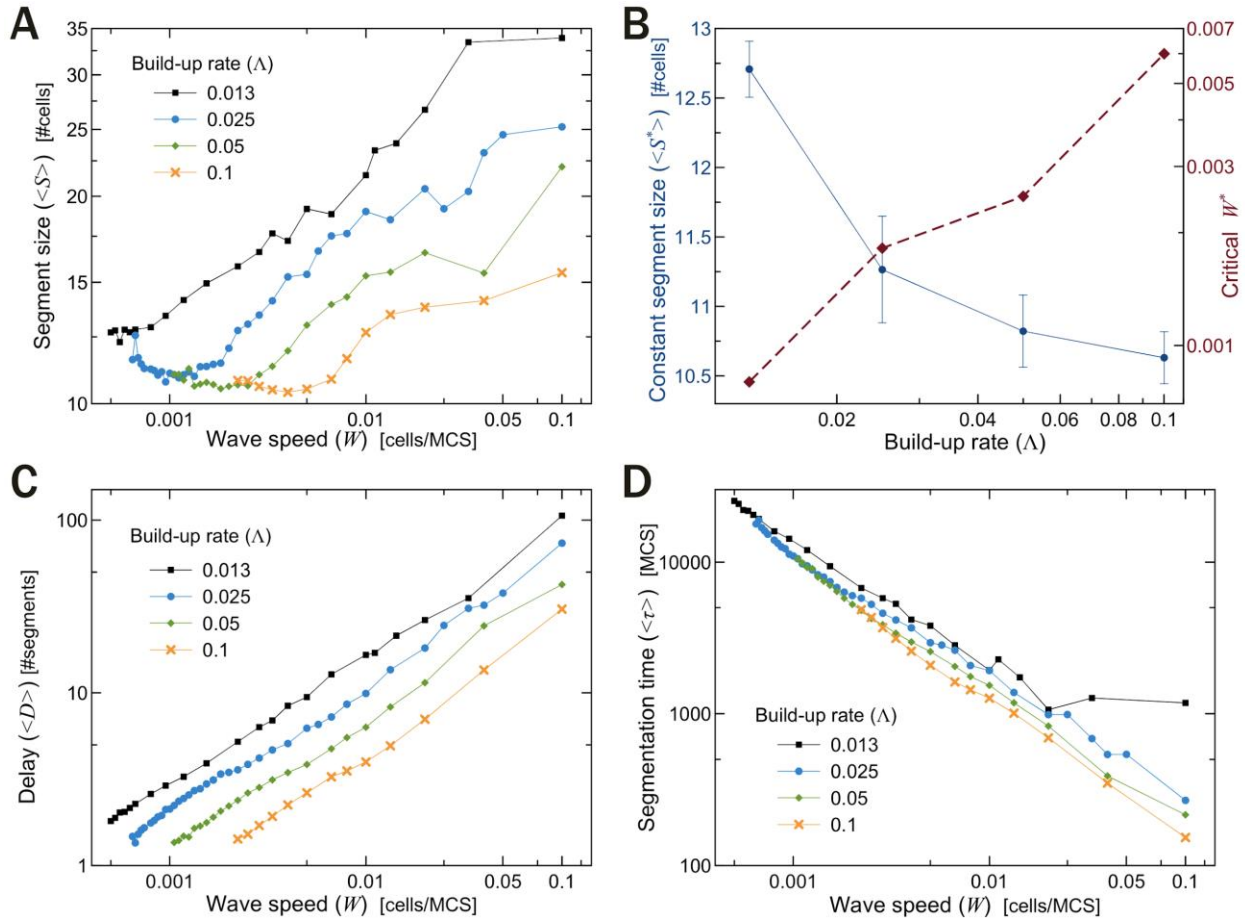
359

360   **Figure 4 - Segmentation as a function of wave speed**

361   (**A**) Average segment size $< S >$ as a function of wave speed W. For slower wave speeds segments are

362   of roughly constant size, but increase as a power law for faster wave speeds. (**B**) Constant segment sizes

363    $< S^* >$ (blue solid line) and critical wave speeds W^* (red dashed line) as functions of Λ. (**C**) Distance

364   between activation and boundary formation $< D >$ increases linearly with W. (**D**) Average segmentation

365   time $< \tau >$ decreases as a power law with $W^{-0.80\pm0.008}$. (**A,C,D**) Each line shows a similar behavior for

366   different base values of the build-up rate of apical contractility (Λ).

367

368   The average distance between cell activation and boundary formation $< D >$ decreased

369   linearly with the build-up rate, as expected: the faster the contractility build-up rate, the

370   less time it takes for segments to form once all cells are actively constricting

371   (Supplemental Figure 3C). The average segmentation time $< \tau >$ was similarly

372   dependent on the build-up rate as on segment size $< S >$, which was expected, given

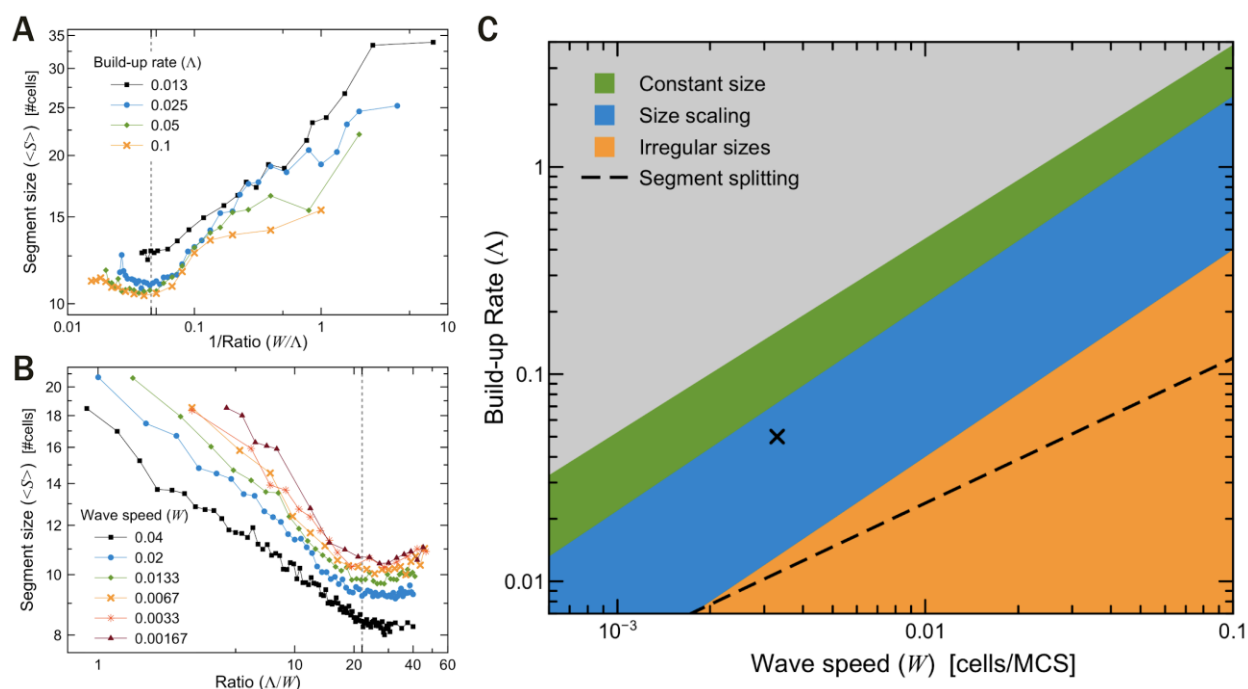373   that $< S >= W < \tau >$ (Supplemental Figure 3D).

374

375   ***Ratio of build-up rate to wave speed sets the transition of scaling regimes***

376

377   The critical values of wave-speed W^* and build-up rate of apical contractility Λ^* for the

378   transition between constant and segment size scaling regimes shown in Figures 4B and

379   Supplemental Figure 3B are related. Rescaling of the horizontal axis in Figures 4A and

380   Supplemental Figure 3A for each curve by their corresponding values of Λ and W,

381   respectively, shows that in both cases, the transition occurs around the same ratio of

382    $\Lambda/W = 22\ MCS^2/cell$ (Figure 5A,B). This allows us to define a boundary transition in

383   parameter space that separates regions where segment sizes change with variations in

384   either Λ or W from regions where the segment sizes remain relatively constant with

385   changes in one of these parameters (Figure 5C, green and blue regions). Note that we

386   use the word *constant* in contrast to the size scaling of the segments with respect to

387   either Λ or W, there is still a small and gradual change in segment sizes within the green

388   region in Figure 5C (see Supplemental Figure 4).

389

390

Figure 5 - Λ/W sets boundaries between segmentation regimes

(**A,B**) Rescaled version of Figures 4A and Supplemental Figure 3A, showing average segment size $< S >$ as a function of (**A**) wave speed to build-up rate, and (**B**) its inverse. Vertical dashed line at $\Lambda/W = 22$ indicate transition threshold between constant size and scaling segment sizes. (**C**) Parameter space diagram showing regions where the combination of the parameters Λ and W leads to constant segment sizes (green), scaling segment sizes (blue), or irregularly sized segments. Black dashed line shows transitions from stable to splitting segments. Black **X** point indicates the reference simulation parameters (see Table 1). Grey region indicates parameters combinations that lead to simulation artifacts.

The parameter space in Figure 5C also contains a grey region where the combinations of Λ and W leads to simulation artifacts (among other things, simulated cells decrease their height by around 10% and neighbouring apical compartments separate from each other without breaking their apical links). All data from this region were discarded in our analysis. The orange region and dashed boundary line will be defined momentarily.

406 ***Segment sizes become irregular for low ratios of build-up rate to wave speed***

407

408 While average segment size increases with higher wave speeds (W) or lower build-up

409 rates of apical contractility (Λ), segment sizes distribution becomes irregular for lower

410 ratios of Λ/W (Figure 6A-D). This can be visualized in plots of segment size variation,

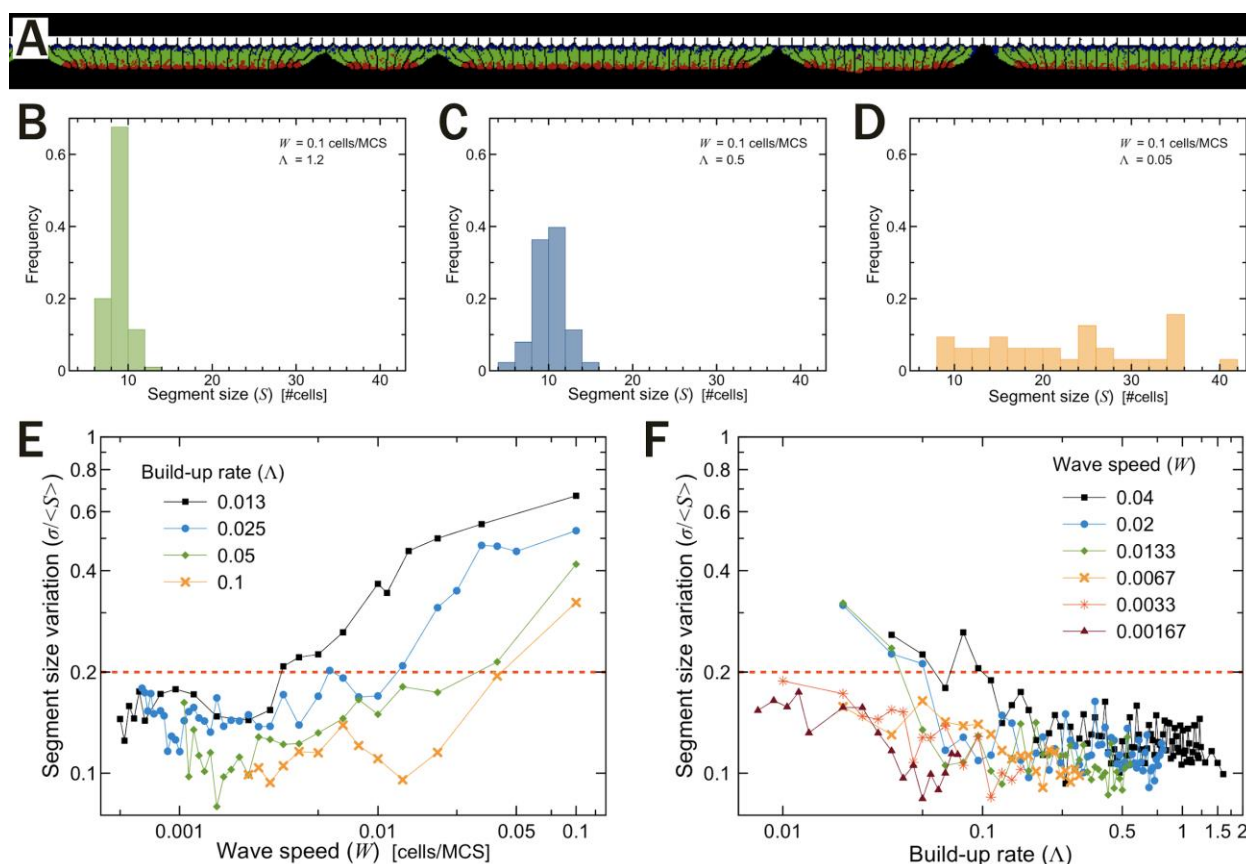411 calculated as the ratio of standard deviation (σ) to the mean ($< S >$) (Figure 6E,F).

412 When the wave speed is much faster than the build-up rate ($W \gg \Lambda$), a large group of

413 cells starts to constrict at about the same time. In this situation, the memory of the last

414 boundary position is erased, and new tissue tears are more likely to appear anywhere in

415 the tissue.

416

417

418 **Figure 6 - Segment size variation**

419 (**A**) Typical simulation output showing wide range of segment sizes from the irregular region (orange) of

420 the parameter space in Figure 5C with W=0.03, $\Lambda = 0.013$. (**B-D**) Histogram of segment size distributions

421 for combinations of Λ and W in the constant size region (**B**), scaling region (**C**), and irregular region (**D**),

422 of the parameter space over 5 trials. (**E**) Segment size variation (std/mean) as a function of build-up rate

423 of apical cytoskeletal activity Λ. (**F**) Segment size variation as a function of wave speed W. (**E,F**) Dashed

424 red lines at $\sigma/< S >= 0.2$ indicate the threshold used to determine the region of irregular segment sizes in

425 Figure 5C.

426

427 We choose to classify segments as irregular when $\sigma/< S >$ is higher than 0.2. This

428 corresponds in our parameter space diagram, to a transition from uniform to non-

429 uniform segments at ratios of $\Lambda/W \leq 4$. A similar dependence on Λ/W is observed with

430 the segmentation time variation ($\sigma/< \tau >$), which measures how uniformly distributed is

431 the time between consecutive boundary formations (see Supplemental Figure 5). A

432 threshold of $\sigma/< \tau >=0.33$ can be similarly used to distinguish between regular and

433 irregular segments. This high variation in segmentation time in the irregular region is

434 expected, as the time taken to form subsequent tears is an emergent output from our

435 mechanical model, rather than a direct input related to the oscillation period of the clock

436 as in the CW model.

437

438 ***Build-up rate and wave speed limit larger segment sizes***

439

440 The above results show that initial segment sizes increase with faster wave speeds

441 (Figure 4A) and slower build-up rates of apical contractility (Supplemental Figure 3A).

442 However, there seems to be a limit on the larger segment sizes. After their initial

443   formation, larger segments are prone to split as the cells within them continue to

444   increase their apical cytoskeletal activity strength (λ_A) and tension keeps building up

445   until a new splitting event occurs near the middle of the formed segment (Figure 7A,B).

446

447   While the occurrence of a splitting event is proportional to the initial segment size

448   (Supplemental Figure 4), the wave speed W has a more direct effect on the frequency

449   of splitting, with higher build-up rates only delaying the appearance of splits (Figure 7D).

450   Together these results suggest that our mechanical model of segmentation sets a

451   higher limit on segment sizes depending on the speed of the wave with respect to the

452   build-up rate of apical cytoskeletal activity (Figure 7C,D). Our results, however, did not

453   point out to a specific ratio of Λ/W as predictive of a transition to a higher frequency

454   (>0.1) of splitting events, but rather a nonlinear function $\Lambda = 0.6 * W^{0.7}$ for the boundary

455   between stable segments and splitting segments (dashed line in Figure 5C).

456
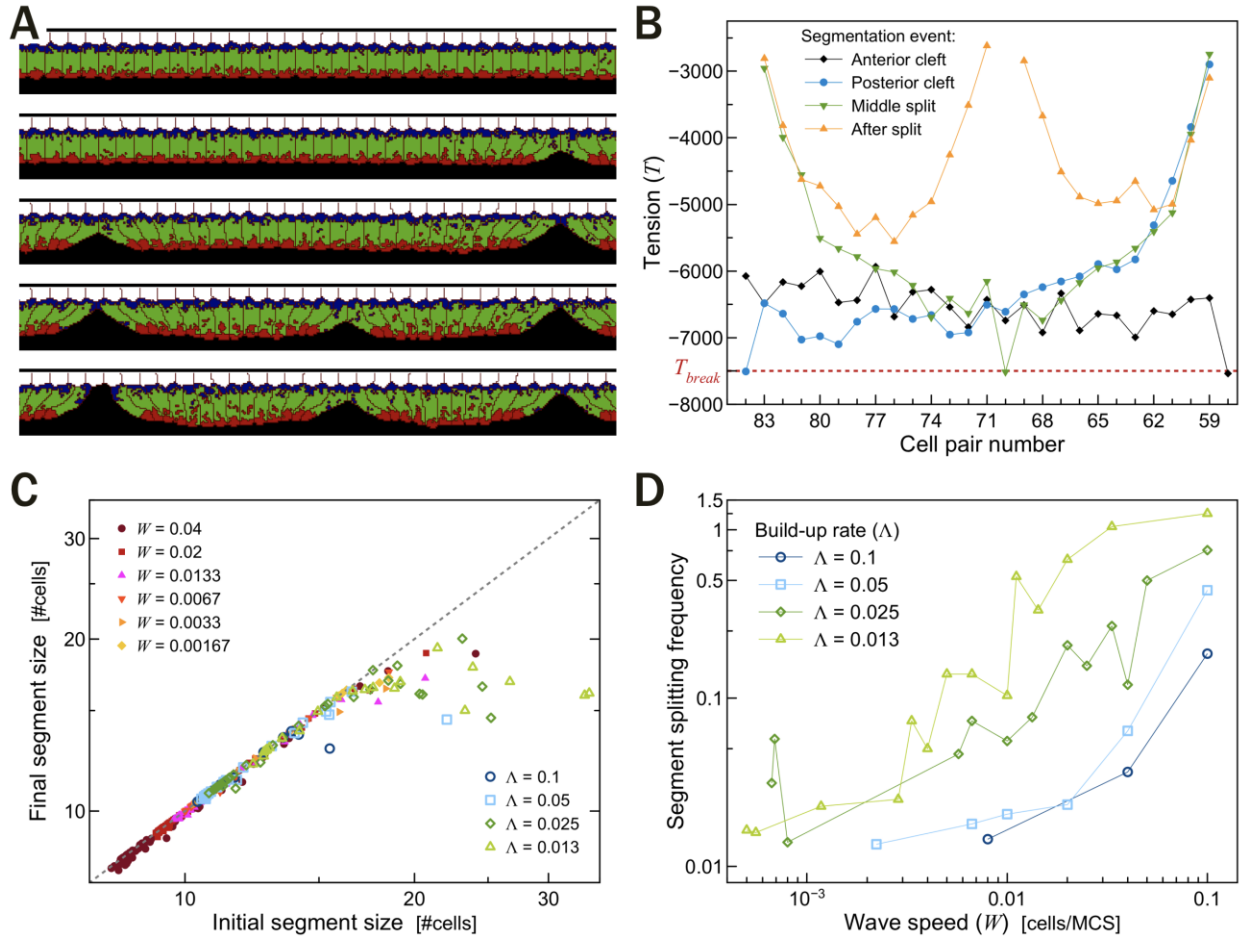
Figure 7 - Splitting of Large Segments

(**A**) Simulation snapshots showing the splitting of a large segment (times, from top to bottom: 47000, 49000, 52000, 54000 and 56500 MCS). (**B**) Evolution of the tension profile for the splitting segment shown in (**A**). (**C**) Plot of average final versus initial segment sizes. Data points at the diagonal gray slashed lines indicate no splitting events. (**D**) Splitting frequency as a function of wave speed W.
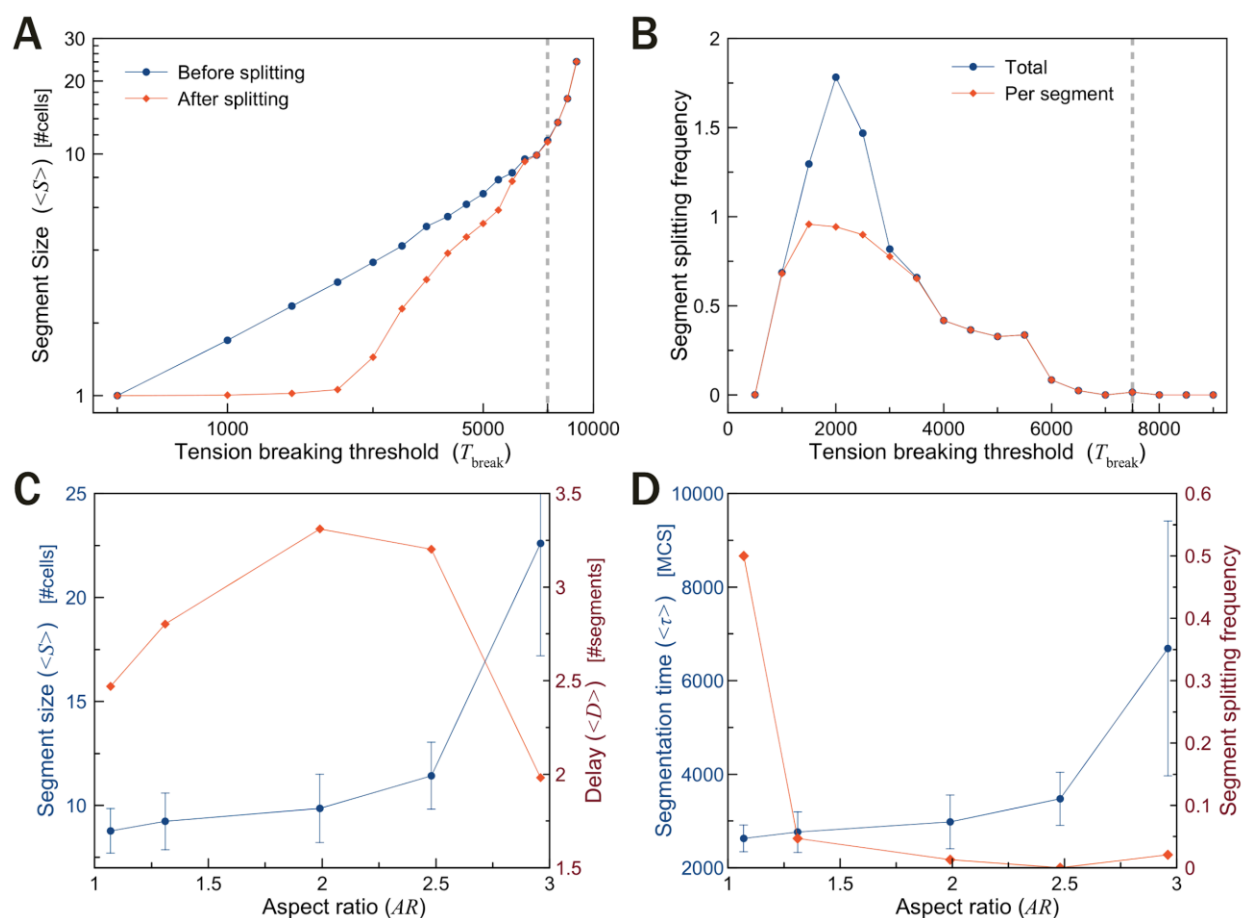
Segment size as a function of maximum tension load

So far, we had used a fixed apical to apical tension breaking threshold of $T_{break} = -7500$. We now test the effects of varying the threshold tension at which the link

469   between the neighboring cells' apical domains break. At the extreme limit of $|T_{break}|$

470   near zero, the average segment contains only one cell. Conversely, at high enough

471   values ($|T_{break}| > 9500$) the tissue never segments and remains a single monolayer. As

472   the magnitude of the breaking threshold increases between these ranges, the average

473   segment sizes also increase, as expected (Figure 8A). Note however, that the splitting

474   frequency is higher for low values of $|T_{break}|$, and zero for high values, with segments

475   breaking in more than once for threshold values around $T_{break} = -2000$ (Figure 8B).

476

477

478   **Figure 8 - Influence of junctional tension limit and cell shape on segmentation**

479   (**A**) Average segmentation size $< S >$ as a function of the absolute value of tension breaking point

480     $|T_{break}|$. Blue lines are initial segment sizes, red lines are segments sizes after splitting. (**B**) Average

481   number of splitting events per segment as a function of $|T_{break}|$. (**C**) Average segmentation size $< S >$

482   (blue) and the distance between activation and boundary formation $< D >$(red) as functions of cell aspect

483   ratio AR. (**D**) Average segmentation time $< \tau >$ (blue) and frequency of segmentation splitting (red) as

484   functions of cell aspect ratio AR.

485

486

487   ***Segmentation as a function of cell shape (aspect ratio)***

488

489   In the pre-somitic tissue, cells elongate dynamically prior and during the process of

490   boundary formation. We had kept the length of the cell fixed for our previous

491   simulations and we now evaluate how segment size depends on the aspect ratio of the

492   cell ($AR = height/width$). Figure 8C shows the average segment size $< S >$ and

493   distance $< D >$ as a function of cell aspect ratio. As expected, it is easier to pack more

494   elongated cells into a segment. The distance $< D >$, however, is a concave curve with

495   respect to AR with a maximum around $AR = 2$. This can be understood as follows: the

496   wider the cells, ($AR < 2$) the harder it is to pack them into a segment made of wedge-

497   shaped cells, so apical tension builds up quickly and tissue separation occurs sooner,

498   thus reducing both the segmentation time (blue line in Figure 8D) and the distance

499   between activation and boundary formation compared to the standard case (Figure 8C).

500   Conversely, the more elongated cells ($AR > 2$), the greater the number of cells that can

501   be packed into a segment and the longer it takes for consecutive boundaries to form.

502   However, since the segments themselves are larger, $< D >$, which is calculated in

503   terms of segment sizes, also decreases. Figure 8D also shows that the segment

504   splitting frequency (red line) is significantly higher for low aspect ratios, which can be

505   understood as a result from the packing constraints that expedites the accumulation of

506   tension between apical cell pairs and make them more prone to splitting.

507

508   **DISCUSSION**

509

510   In this paper, we describe a mechanical model of tissue segmentation where a

511   continuous wave of apical constriction activation coupled with maximum apical tension

512   load sets the position of future somite boundaries. The model is based on experimental

513   observations of extensive cell rearrangements during somite formation [17],

514   observations with somitomeres [21-22] and our own SEM images (Figure 1A)

515   suggesting that the segmentation process begins dorsally in the PSM at least 4 somite

516   lengths prior to the formation of the last somite. We interpreted the spatial segmentation

517   of the dorsal epithelium into similarly sized cohorts of cells as the result of an increased

518   longitudinal (rostral-caudal) tension between the cells.

519

520   A similar process is known to cause the appearance of periodic cracks on non-biological

521   thin films subjected to tensile stress [35-36]. Analysis of these films show that the

522   spacing between these cracks depends on the stress, thickness and toughness of the

523   film. In these models, however, the stress is usually assumed to be uniform, non-time

524   varying, and applied externally to the material. One exception is the work by Yuse and

525   Sano, where a time-varying inhomogeneous thermal stress was applied to a plate

526   moving between two reservoirs [37-38]. The velocity of the plate and the temperature

527   difference between the two reservoirs act as control parameters and define a phase

528   space where periodic cracks could transition into other morphologies. Our model on

529   pre-somitic tissue segmentation differs from these analogies in two ways, firstly, the

530   material is ductile, and secondly and mostly importantly, the material is not

531   homogeneous, but subdivided into discrete units (the cells).

532

533   In biology, mechanical forces generated by fibroblasts have been shown to assist in the

534   remodeling of the external collagen matrix to form self-organized tissue structures [39].

535   Tensile stresses generated by stretching fibroblasts suspended in collagen and

536   restrained by a glass mesh have also been known to result in aggregations of cells .

537   The self-organization of cells into clusters in the absence of chemical signals led Harris

538   and colleagues to suggest that mechanical instabilities could act as sources of

539   positional information instead of diffusible factors like morphogens [40]. More recently

540   the possibility of mechanical instabilities resulting in vertebrate segmentation has also

541   been explored by Truskinovsky and colleagues [41]. Assuming relaxation of junctional

542   adhesion sites as the PSM elongates, the model identifies that the number of somites

543   generated by their pre-patterning mechanism is robust to the final segmentation

544   process. Their static model, however, neglects the sequential development of the

545   boundaries and does not take into account any active processes within the tissue.

546

547   Given these differences we developed our own model of epithelial segmentation where

548   we identified four key parameters: the speed of the wave (W), the rate of increase of

549   apical contractility (Λ), the maximum apical cell-cell junction load (T_{break}), and the

550   aspect ratio of the cells (AR) (Table 1). While the parameters have been chosen to

551   imitate segment size in chicken, we comment that we need better tuning of the aspect

552   ratio of the cells in the dorsal region, where we found that cells can reach aspect ratios

553   as high as 7. To compare results at these higher aspect ratios we would require re-

554   parametrizing our cell volume to allow for sufficient apical surface so that the width is

555   much greater than a chosen L_{AT}. While these changes are easily programmable, they

556   come at a greater computational cost.

557

558   Other possible explanatory models include a cell clustering model (Figure 1E). Here we

559   assume that the dorsal cells are initially confluent, but not tightly connected at their

560   apical sides. As a wavefront of maturation passes, cells start to connect with their

561   neighbors and condense initially into small groups, later clustering into larger, more

562   tightly connected cohorts that eventually pattern the dorsal tissue into distinct tissue

563   segments. Alternatively, instead of a continuous wavefront of activation/maturation, both

564   processes (apical constriction and cell clustering) can be initiated at the center of the

565   future segment by a small group of cells that eventually recruit and/or activate their

566   neighbors (Figure 1F). This mechanism of initiation still assumes some kind of caudally

567   moving wavefront, but also requires some positioning mechanism that may be provided

568   as an earlier clock read-out. All those models, including the mechanical instability model

569   explored here, provide an initial segmentation pattern that would later guide the

570   formation of the full somite as the epithelialization process spreads to the ventral,

571   medial and lateral sides of each forming epithelial sphere. These processes assume

572   some kind of wavefront but are in principle independent of a clock, which is necessary

573   for the molecular patterning of the somites into caudal and rostral identities [15].

574

575   We found that our purely mechanical model (Figure 1D) is able to produce spatially and

576   temporally regular segment sizes. Similar to the CW models, segment sizes scale

577   (increase) with higher wave speeds as seen in many species (Figure 4A). We found,

578   however, that this scaling is not linear with wave speeds, as would be expected from a

579   simple deterministic version of the CW model. There are two limits to this scaling

580   behavior, which can be characterized by Λ/W ratios alone (Figure 5C). An upper limit in

581   segment sizes is reached for low ratios ($\Lambda/W < 4$), where initially formed segments are

582   prone to splits due to mechanical instabilities; and a lower limit in the sizes is reached

583   for high ratios ($\Lambda/W > 22$), where segment sizes do not scale with wave speeds. These

584   limits in somite size are absent in CW models and offer an explanation for the observed

585   splitting of large somites formed in some perturbation experiments [42-43].

586   Segmentation time in our model is not imposed but rather calculated as the difference in

587   time for the appearance of the rostral and caudal boundaries. We find that it decreases

588   with wave speeds and is insensitive to build-up rates (Figures 4D, 5D).

589

590   Our model predicts that disruptions in the protein levels of molecules (eg myosin, actin)

591   that control the apical contractility of the PSM cells will affect the distributions of

592   segment sizes. Upregulating these molecules will have a similar effect as increasing λ_A

593   (Fig 2C), leading to smaller segments. However, since the segment sizes in our model

594   is also dependent on the sequential rostral-caudal activation of these molecules, we

595   expect cases in which for a fixed tension load, segment sizes could become

596   independent of the protein activity (similar to constant segment sizes in Fig 5C). Any

597 disruptions on the strength of the adhesion junctions between the PSM cells (equivalent

598 to lowering T_{break} in our model) will also lead to smaller segments. We also comment

599 that experiments with a continuous growing tissue as in [41] will differ from a fixed tissue

600 model, as in the former case we will expect a reduction in the strength of apical links λ_A,

601 leading to larger segment sizes.

602

603 Our model seems to have higher variations in the distribution of the segment sizes and

604 formation time than existing mathematical implementations of the clock-and-wavefront

605 model [14]. In a real 3D scenario however, epithelialization along the dorsal sides does

606 not happen along a line as in our model, but within a plane that also extends along the

607 medial-lateral direction. Addition of these neighboring cells into our model would likely

608 reduce variation in segment size and segmentation time.

609

610 While our mechanical model drastically differs from the CW family of models with

611 respect to the absence of an intracellular molecular clock within prospective somite

612 cells, it still assumes the presence of some sort of caudally travelling wave, which does

613 not need to be the same as the one postulated by the CW. We are agnostic about the

614 nature of this wave, which can be either a cell-autonomous maturation process (starting

615 from their addition to the tail-bud or a similar event), a tissue level processes, such as a

616 read-out of FGF and RA levels, or a combination of both [44]. As is often the case in

617 biology, we speculate that mechanics and molecular based oscillatory signaling may

618 work together to yield a robust morphological outcome.

619

620 Our current model, however, is too simple to explore such scenarios as it is restricted to

621 a 1D view of the dorsal monolayer and is aimed to reproduce segmentation events prior

622 to the formation of a full somite. Further developments of this basic model will include

623 the self-organization of the PSM cells ventral to the dorsal monolayer and the expansion

624 of the model to 3D. It is known that in chicken [17] different regions of the PSM

625 epithelialize at different times, and it would be interesting to explore the implications of

626 these observations in an augmented version of the mechanical model presented here.

627

628 **COMPUTATIONAL MODELS**

629

630 ***Linear elastic model***

631

632 We implement the interaction of adjacent cells as a series of springs of time-varying strength

633 $\lambda_i(t)$ and resting length x_0, connecting a chain of N point objects. While the number of cells is

634 finite, we set it large enough ($N = 50$) such that in the time scale we consider, there are no

635 significant edge effects and the chain is effectively infinite. Our model creates motion by linearly

636 increasing the spring constant over time at a fixed rate (Λ) from a minimum value k_0 to a

637 maximum value k_{max}, with a delay (or wave speed W) based on how far along the chain the

638 spring is. At each time step, the acceleration due to spring forces is calculated and used to set

639 up a system of $2N$ first order ODEs with time dependent coefficients. This time dependence

640 means there is no practical way to solve this system analytically and we use MATLAB Ode45 to

641 solve numerically how the cells interact over time. This is the simplest way to model this

642 behavior since there are no random elements, and therefore this model cannot account for

643 possible effects of viscosity or thermal fluctuations. However it means that the results we do get

644 are precise and replicable.

645

646   Along with positions and velocities, tension in each spring is tracked over time. At each step, the

647   tension of each spring is checked. If the spring exceeds a predetermined threshold tension

648   (T_{break}), the spring constant is set to zero for the remainder of the calculation, effectively

649   breaking the spring. The time and location of each break is recorded.

650

651   At any given time, the acceleration of a point x_i connected by two springs is given by:

652

653   (Eq. X1) $a_i(t) = \lambda_i(t) * (x_{i+1}(t) - x_i(t) - x_0) - \lambda_{i-1}(t) * (x_i(t) - x_{i-1}(t) - x_0)$

654

655   Here t is time, i is the cell position number, and $a_1 = a_N = 0$, fixing the endpoints. Fixing the

656   end could theoretically cause edge effects but the chain is long enough so that that first break

657   always occurs before any wave behavior could reflect back into the system.

658

659   The spring constant and tensions at each cell neighboring pair are:

660

661   (Eq. X2) $\lambda_i(t) = min\left(k_{max}, \ k_0 + \Lambda * \left(t - \frac{i}{W}\right) * \Theta\left(t - \frac{i}{W}\right)\right)$

662

663   (Eq. X3) $T_i(t) = \lambda_i(t) * (x_{i+1}(t) - x_i(t) - x_0)$

664

665   Where Θ is the Heaviside function.

666

667   ***CPM/GGH model***

668

669   We implement our full model as a simulation using the Cellular Potts (CPM), or Glazier-Graner-

670   Hogeweg (GGH) model [23] written using the open-source CompuCell3D simulation

671   environment [24]. The CPM/GGH framework represents each cell, or cell region as a collection

672   of voxels that forms a domain within a fixed grid (here, square). An effective energy defines

673   cell/domain properties such as size, mobility, adhesion preferences and distance constraints

674   with other domains:

675

676   (Eq. 1) $H = H_0 + H_V + H_I + H_A + H_B,$

677

678   where we defined each term below.

679

680   The initial configuration of all cells/domains evolve in time by a series of random neighboring

681   pixel copy attempts whose acceptance is governed by a Metropolis algorithm, with a number of

682   pixel-flips equal to the grid size defining the time unit of the simulation, a Monte Carlo Step

683   (MCS).

684

685   Similar to what has been done in previously models [15,25], each cell is composed of 3 domains

686   representing the apical, basal and core regions of an epithelial cell. The size of the domains is

687   maintained by a volume constraint in the Hamiltonian:

688

689   (Eq. 2) $H_{Volume} = H_V = \sum_\sigma \lambda_V (V(\sigma) - V_T(\sigma))^2,$

690

691   where the sum is over all domains (σ), $V(\sigma)$ is the current cell volume, $V_T(\sigma)$ is the cell target

692   volume, and λ_V is a lagrangian multiplier setting the strength of the constraint.

693

694   We defined the cell aspect ratio AR to be the ratio of apical/basal length to cell width. This ratio

695   is maintained through spring-like distance constraints between the centers of mass of the three

696   domains belonging to each cell:

697

698   (Eq. 3) $H_{Internal\ Links} = H_I = \sum_{\sigma,\sigma'} \lambda_I (L(\sigma,\sigma') - L_{IT}(\sigma,\sigma'))^2,$

699

700   where the sum is taken over the three pairs of domains within each cell, $L(\sigma,\sigma')$ is the current

701   distance between the center of mass of the two domains, $L_{IT}(\sigma,\sigma')$ is the corresponding target

702   distance, and λ_I is the strength of the constraint. To prevent cells from bending we set the target

703   distance between apical and basal domains equal to the sum of the target distance between the

704   core domain to the apical and basal domains.

705

706   Adhesion between cells is modeled with the standard Potts model internal energy term:

707

708   (Eq. 4) $H_{Adhesion} = H_0 = \sum_{i,j} J(\sigma_i, \sigma_j),$

709

710   where the sum is taken over all fourth-order neighboring pairs of grid coordinates i and j; σ_i and

711   σ_j are the cell domains at grid coordinates i and j, respectively; and J is the contact energy per

712   unit area between those domains.

713

714   Apical constriction is a cell autonomous process that may lead to tissue-level events, such as

715   invagination, through the coupling of the internal contractile activity of actin-myosin cytoskeleton

716   of neighboring cells with their adhesion junctions. Since we are interested only on the tissue

717   level effects of this process, we model junctional adhesion and apical constriction similar to (Eq.

718   3), with a distance constraint between neighboring apical domains:

719

720   (Eq. 5) $H_{Apical\ links} = H_A = \sum_{\sigma,\sigma'} \lambda_A(\sigma,\sigma')(L(\sigma,\sigma') - L_{AT})^2,$

721

722   where the sum is taken over all pairs of neighboring apical domains, $L(\sigma,\sigma')$ is the current

723   distance between their center of mass, L_{AT} is the target distance between them, and $\lambda_A(\sigma,\sigma')$ is

724   the time-varying strength of the constraint. The target distance between neighboring apical

725   domains is constant throughout the simulations and set to 3 pixels, a value much shorter than

726   the initial width of the cells (10 pixels). Initially the constraint $\lambda_A(\sigma,\sigma')$, which we interpret here

727   as the combined strength of apical cytoskeletal activity between cell pairs, is set very low ($\lambda_A =$

728   20), so that there is no effect on the tissue or individual cell shapes. A similar form ($H_{Basal\ links}$)

729   is used for neighbouring basal domains with a fixed $\lambda_B = 100$. This term ensures that the top

730   part of the tissue stays together once the apical compartments have separated.

731

732   Above the basal side of cells, there is a collection of domains representing the ectoderm and

733   fibronectin- and laminin-rich extracellular matrix that forms a basal lamina [26]. These domains

734   have a volume constraint and liable adhesion with the basal side of the epithelial cells that helps

735   to maintain the alignment of the cells below them, while allowing some upward/downward

736   movement of the cells. Below their apical sides, cells are adjacent to a loose mesenchyme

737   (mainly corresponding to the future "core" of the somite, or somitocoel) which we choose to

738   model as a single domain with no volume constraint and labile adhesion to the cells.

739

740   At the rostral and caudal ends of the row of cells, we include a single immotile cell, which does

741   not change in shape or properties over time. Between them there are 115 to 205 cells,

742   depending on the conditions being tested in the simulations. Apart from the fixed cells that make

743   the AP boundaries, all cells have identical properties and are allowed to change shape and

744   properties during the course of the simulation.

745

746   Initially all cells are in an inactive state, without exerting significant forces on each other. We

747   define a 'wave of constriction activation' which moves through the tissue from the rostral end at

748   a fixed speed W (in units of cell/MCS), so that the next caudal cell is activated $1/W$ MCS after

749   the lastly activated cell. Apical constriction results from a linear increase in λ_A between a pair of

750   activated cells. This variable varies from an initial value of 20 up to 600 at a specific build-up

751   rate $\Lambda = d\lambda_A/dt$ (in units of 1/MCS). As λ_A increases, the tension between a pair of cell's apical

752   domains is:

753

754   (Eq. 6) $T(\sigma, \sigma') \ = \ -2\,\lambda_A(L(\sigma, \sigma') - L_{AT})$

755

756   When this tension value exceeds a maximum threshold $T_{break} = -7500$ the link between the

757   apical domains of neighboring cells is broken, resulting in the apical separation between the cell

758   pairs.

759

760   Variation in cell aspect ratios was implemented by adjusting the internal distance constraints

761   between domains in Eq. 3. We also choose to keep the total sum of all domain target volumes

762   constant and adjust the initial width and length of the cells to satisfy the internal distance

763   constraints.

764

765   ***Reference Simulation Parameters***

766

767   Our simulations have 4 parameters, which we will vary systematically in this study:

768   1) *the wave speed W*, at which the constriction front travels from the rostral to the caudal

769   end of the tissue. The position of the front determines when and where cell pairs start

770   increasing λ_A;

771   2) *the rate of increase of apical contractility (build-up rate)* $\Lambda = d\lambda/dt$, which determines

772   how fast the cell pair λ_A increases once activated;

773   3) *the apical tension breaking threshold T_{break}*, which determines the tension (Eq. 6) at

774   which apical links between neighboring cells break (Eq. 5); and

775   4) *the cell aspect ratio AR*, which defines how elongated the cells are at the beginning of

776   the simulation.

777

778 The reference values of all 4 parameters can be found in (Table 1). Rest of the simulation

779 parameters are listed in the Supplementary Materials.

780

Parameter	Symbol	Base value (units)
Wave speed	W	0.003 (cells/MCS)
Apical contractility build-up rate	Λ	0.05 (MCS^{-1})
Apical tension breaking threshold	T_{break}	-7500 (dimensionless)
Cell aspect ratio (height/width)	AR	2 (dimensionless)

781 **Table 1 - Reference values of the 4 key parameters of our model.**

782

783 ***Metrics***

784

785 To analyze the behavior of our model with respect to variation in key parameters we define and

786 measure the following metrics:

    1) *Average Segment Size* $<S>$: defined as the mean number of cells within each cohort in

788   our simulations. We measure the sizes both during the course of the simulation - by

789   taking into account the first occurrence of a separation located caudal to the caudal-most

790   segment - and at the end of the simulation in order to assess the presence of any

791   splitting events.

792   2) *Average Distance* $<D>$: defined as the distance between the last activated cell pair

793   and the last formed boundary of apical link breakage. This metric is measured during the

794   course of the simulation and is presented in units of the average segment size $<S>$ for

795   the corresponding set of parameters.

796   3) *Average Segmentation Time* $<\tau>$: defined as the time (in MCS units) elapsed between

797   the appearance of two consecutive boundaries.

798

799 To avoid boundary effects, all parameters are measured after the appearance of the first

800 segmentation and before a distance of $3<S>$ from the last formed segment from the rostral

801 boundary.

802

803

804 **ACKNOWLEDGMENTS**

805

809

810

811

REFERENCES

1. Pourquié, O. (2001). Vertebrate Somitogenesis. Annu Rev Cell Dev Biol, 17:311-50. https://doi.org/10.1146/annurev.cellbio.17.1.311

2. Christ, B., & Ordahl, C. P. (1995). Early stages of chick somite development. Anatomy and Embryology, 191(5), 381–396. https://doi.org/10.1007/BF00304424

3. Cooke, J. (1975). Control of somite number during morphogenesis of a vertebrate, Xenopus laevis. Nature, 254(5497), 196–199. https://doi.org/10.1038/254196a0

4. Snow, M.H., Tam, PP. (1979). Is compensatory growth a complicating factor in mouse teratology? Nature, 279(5713), 555-557. https://doi.org/10.1038/279555a0

5. Stern, C. D., Fraser, S. E., Keynes, R. J., & Primmett, D. R. N. (1988). A cell lineage analysis of segmentation in the chick embryo. Development, 104(SUPPL.), 231–244.

6. Primmett, D. R. N., Norris, W. E., Carlson, G. J., Keynes, R. J., & Stern, C. D. (1989). Periodic segmental anomalies induced by heat shock in the chick embryo are associated with the cell cycle. Development, 105(1), 119–130.

7. Collier, J. R., Mcinerney, D., Schnell, S., Maini, P. K., Gavaghan, D. J., Houston, P., & Stern, C. D. (2000). A cell cycle model for somitogenesis: Mathematical formulation and numerical simulation. Journal of Theoretical Biology, 207(3), 305–316. https://doi.org/10.1006/jtbi.2000.2172

8. Meinhardt, H. Models of Biological Formation. 2nd ed. London: Academic Press; 1982.

9. Cotterell, J., Robert-Moreno, A., & Sharpe, J. (2015). A Local, Self-Organizing

Reaction-Diffusion Model Can Explain Somite Patterning in Embryos. Cell

Systems, 1(4), 257–269. https://doi.org/10.1016/j.cels.2015.10.002

10. Cooke, J., & Zeeman, E. C. (1976). A clock and wavefront model for control of the

number of repeated structures during animal morphogenesis. Journal of

Theoretical Biology, 58(2), 455–476. https://doi.org/10.1016/S0022-

5193(76)80131-2

11. Palmeirim, I., Henrique, D., Ish-Horowicz, D., & Pourquié, O. (1997). Avian hairy

gene expression identifies a molecular clock linked to vertebrate segmentation and

somitogenesis. Cell, 91(5), 639–648. https://doi.org/10.1016/S0092-

8674(00)80451-1

12. Hester, S. D., Belmonte, J. M., Gens, J. S., Clendenon, S. G., & Glazier, J. A.

(2011). A multi-cell, multi-scale model of vertebrate segmentation and somite

formation. PLoS Computational Biology, 7(10).

https://doi.org/10.1371/journal.pcbi.1002155

13. Tiedemann, H. B., Schneltzer, E., Zeiser, S., Hoesel, B., Beckers, J., Przemeck,

G. K. H., & de Angelis, M. H. (2012). From dynamic expression patterns to

boundary formation in the presomitic mesoderm. PLoS Computational Biology,

8(6). https://doi.org/10.1371/journal.pcbi.1002586

14. Baker, R. E., Schnell, S., & Maini, P. K. (2006). A clock and wavefront mechanism

for somite formation. Developmental Biology, 293(1), 116–126.

https://doi.org/10.1016/j.ydbio.2006.01.018

15. Dias, A. S., De Almeida, I., Belmonte, J. M., Glazier, J. A., & Stern, C. D. (2014).

Somites without a clock. Science, 343(6172), 791–795.

858   https://doi.org/10.1126/science.1247575

859   16. Nelemans, B. K. A., Schmitz, M., Tahir, H., Merks, R. M. H., & Smit, T. H. (2020).

860   Somite Division and New Boundary Formation by Mechanical Strain. *IScience*,

861   *23*(4), 100976. https://doi.org/10.1016/j.isci.2020.100976

862   17. Martins, G. G., Rifes, P., Amaândio, R., Rodrigues, G., Palmeirim, I., &

863   Thorsteinsdóttir, S. (2009). Dynamic 3D cell rearrangements guided by a

864   fibronectin matrix underlie somitogenesis. PLoS ONE, 4(10).

865   https://doi.org/10.1371/journal.pone.0007429

866   18. Duband, J. L., Dufour, S., Hatta, K., Takeichi, M., Edelman, G. M., & Thiery, J. P.

867   (1987). Adhesion molecules during somitogenesis in the avian embryo. Journal of

868   Cell Biology, 104(5), 1361–1374. https://doi.org/10.1083/jcb.104.5.1361

869   19. Bénazéraf, B., Francois, P., Baker, R. E., Denans, N., Little, C. D., & Pourquié, O.

870   (2010). A random cell motility gradient downstream of FGF controls elongation of

871   an amniote embryo. Nature, 466(7303), 248–252.

872   https://doi.org/10.1038/nature09151

873   20. Mongera, A., Rowghanian, P., Gustafson, H. J., Shelton, E., Kealhofer, D. A.,

874   Carn, E. K.,Campàs, O. (2018). A fluid-to-solid jamming transition underlies

875   vertebrate body axis elongation. Nature, 561(7723), 401–405.

876   https://doi.org/10.1038/s41586-018-0479-2

877   21. Meier, S. (1979). Development of the chick embryo mesoblast: Formation of the

878   embryonic axis and establishment of the metameric pattern. *Developmental*

879   *Biology*, *73*(1), 25–45. https://doi.org/10.1016/0012-1606(79)90135-0

880   22. Tam, P. P. L., Meier, S., & Jacobson, A. G. (1982). Differentiation of the Metameric

881   Pattern in the Embryonic Axis of the Mouse: II. Somitomeric Organization of the

882   Presomitic Mesoderm. *Differentiation*, *21*(1–3), 109–122.

883   https://doi.org/10.1111/j.1432-0436.1982.tb01203.x

884   23. Graner, F., & Glazier, J. A. (1992). Simulation of biological cell sorting using a two-

885   dimensional extended Potts model. *Physical Review Letters*, *69*(13), 2013–2016.

886   https://doi.org/10.1103/PhysRevLett.69.2013

887   24. Swat, M. H., Thomas, G. L., Belmonte, J. M., Shirinifard, A., Hmeljak, D., &

888   Glazier, J. A. (2012). Multi-Scale Modeling of Tissues Using CompuCell3D. In

889   Methods in Cell Biology (Vol. 110). https://doi.org/10.1016/B978-0-12-388403-

890   9.00013-8

891   25. Belmonte, J. M., Clendenon, S. G., Oliveira, G. M., Swat, M. H., Greene, E. V.,

892   Jeyaraman, S., Bacallao, R. L. (2016). Virtual-Tissue computer simulations define

893   the roles of cell adhesion and proliferation in the onset of kidney cystic disease.

894   *Molecular Biology of the Cell*, *27*(22), 3673–3685. https://doi.org/10.1091/mbc.E16-

895   01-0059

896   26. Rifes, P., Carvalho, L., Lopes, C., Andrade, R. P., Rodrigues, G., Palmeirim, I., &

897   Thorsteinsdóttir, S. (2007). Redefining the role of ectoderm in somitogenesis: A

898   player in the formation of the fibronectin matrix of presomitic mesoderm.

899   *Development*, *134*(17), 3155–3165. https://doi.org/10.1242/dev.003665

900   27. Stern, C. D., & Piatkowska, A. M. (2015). Multiple roles of timing in somite

901   formation. Seminars in Cell and Developmental Biology, 42, 134–139.

902   https://doi.org/10.1016/j.semcdb.2015.06.002

903   28. Baker, P. C., & Schroeder, T. E. (1967). Cytoplasmic filaments and in the

904   amphibian. Developmental Biology, 15, 432–450.

905   29. Pilot, F., & Lecuit, T. (2005). Compartmentalized morphogenesis in epithelia: From

906   cell to tissue shape. Developmental Dynamics, 232(3), 685–694.

907   https://doi.org/10.1002/dvdy.20334

908   30. Martin, A. C., & Goldstein, B. (2014). Apical constriction: Themes and variations on

909   a cellular mechanism driving morphogenesis. Development (Cambridge), 141(10),

910   1987–1998. https://doi.org/10.1242/dev.102228

911   31. Sawyer, J. M., Harrell, J. R., Shemer, G., Sullivan-Brown, J., Roh-Johnson, M., &

912   Goldstein, B. (2010). Apical constriction: A cell shape change that can drive

913   morphogenesis. Developmental Biology, 341(1), 5–19.

914   https://doi.org/10.1016/j.ydbio.2009.09.009

915   32. Pearl, E. J., Li, J., & Green, J. B. A. (2017). Cellular systems for epithelial

916   invagination. Philosophical Transactions of the Royal Society B: Biological

917   Sciences, 372(1720), 0–3. https://doi.org/10.1098/rstb.2015.0526

918   33. Martin, A. C., Gelbart, M., Fernandez-Gonzalez, R., Kaschube, M., & Wieschaus,

919   E. F. (2010). Integration of contractile forces during tissue invagination. Journal of

920   Cell Biology, 188(5), 735–749. https://doi.org/10.1083/jcb.200910099

921   34. Manning, L. A., Perez-Vale, K. Z., Schaefer, K. N., Sewell, M. T., & Peifer, M.

922   (2019). The Drosophila Afadin and ZO-1 homologues Canoe and Polychaetoid act

923   in parallel to maintain epithelial integrity when challenged by adherens junction

924   remodeling. *Molecular Biology of the Cell*, *30*(16), 1938–1960.

925   https://doi.org/10.1091/mbc.E19-04-0209

926   35. Thouless, M.D. Crack Spacing in Brittle Films on Elastic Substrates. (1990) Journal

927   of the American Ceramic Society. 73(7), 2144-46

928   36. Thouless, M. D., Li, Z., Douville, N. J., & Takayama, S. (2011). Periodic cracking of

929   films supported on compliant substrates. *Journal of the Mechanics and Physics of*

930   *Solids*, *59*(9), 1927–1937. https://doi.org/10.1016/j.jmps.2011.04.009

931   37. Yuse, A., & Sano, M. (1993). Transition between crack patterns in quenched glass

932   plates. *Nature*, *362*(6418), 329–331. https://doi.org/10.1038/362329a0

933   38. Yuse, A., & Sano, M. (1997). Instabilities of quasi-static crack patterns in quenched

934   glass plates. *Physica D: Nonlinear Phenomena*, *108*(4), 365–378.

935   https://doi.org/10.1016/S0167-2789(97)00011-0

936   39. Stopak, D., & Harris, A. K. (1982). Connective tissue morphogenesis by fibroblast

937   traction. I. Tissue culture observations. *Developmental Biology*, *90*(2), 383–398.

938   https://doi.org/10.1016/0012-1606(82)90388-8

939   40. Harris, A. K., Stopak, D., & Warner, P. (1984). Generation of spatially periodic

940   patterns by a mechanical instability: A mechanical alternative to the Turing model.

941   *Journal of Embryology and Experimental Morphology*, *VOL. 80*, 1–20.

942   41. Truskinovsky, L., Vitale, G., & Smit, T. H. (2014). A mechanical perspective on

943   vertebral segmentation. International Journal of Engineering Science, 83, 124–137.

944   https://doi.org/10.1016/j.ijengsci.2014.05.003

945   42. Stern, C. D., & Bellairs (1984). The roles of node regression and elongation of the

946   area pellucida in the formation of somites in avian embryos. *Development*, 81, 75–

947   92 https://doi.org/10.1126/science.1075544

948   43. Cooke, J. (1978). Somite abnormalities caused by short heat shocks to pre-neurula

949   stages of Xenopus laevis. *Journal of Embryology and Experimental Morphology*,

950   *VOL. 45*, 283–294.

951   44. Dubrulle, J., McGrew, M. J., & Pourquié, O. (2001). FGF signaling controls somite

952   boundary position and regulates segmentation clock control of spatiotemporal Hox

953   gene activation. *Cell*. https://doi.org/10.1016/S0092-8674(01)00437-8

954

955